UARS/MLS Cloud Ice Measurements: Implications for H_2O Transport near the Tropopause

D. L. WU AND W. G. READ

Jet Propulsion Laboratory, California Institute of Technology, Pasadena, California

A. E. DESSLER

Earth System Science Interdisciplinary Center, University of Maryland, College Park, College Park, Maryland

S. C. SHERWOOD

Department of Geology and Geophysics, Yale University, New Haven, Connecticut

J. H. JIANG

Jet Propulsion Laboratory, California Institute of Technology, Pasadena, California

(Manuscript received 22 October 2003, in final form 27 March 2004)

ABSTRACT

A technique for detecting large hydrometeors at high altitudes is described here and applied to the *Upper Atmosphere Research Satellite*/Microwave Limb Sounder (*UARS*/MLS) 203-GHz radiance measurements at tangent pressures between 200 and 46 hPa. At these tangent pressures the radiances remain optically thin and cloudy-sky radiances are brighter than normal clear-sky cases. Unlike infrared/visible cloud observations, the 203-GHz radiances can penetrate most ice clouds and are sensitive to ice crystals of convective origin. Rough ice water content (IWC) retrievals are made near the tropopause using estimated size distributions from in situ convective studies. The seasonal mean IWC observed at 100 hPa reaches vapor-equivalent 20 ppmv or more over convective centers, dominating the total water content. Convectively lofted ice, therefore, appears to be hydrologically significant at the tropical cold point. IWC is well correlated spatially with relative humidity with respect to ice (RH_i) at 100 hPa during both the dry (January–March) and moist (July–September) periods.

1. Introduction

Clouds near the tropical tropopause layer (TTL) play an important role in the water budget in the earth's upper troposphere. However, lack of cloud and water vapor measurements has been a major limitation in understanding what this role is. In particular, the role of overshooting, convective clouds near the tropical tropopause has been contested in the literature (e.g., Newell and Gould-Stewart 1981; Danielsen 1982; Dessler 1998; Sherwood and Dessler 2000; Holton and Gettelman 2001).

Measuring cloud ice at the tropopause altitudes has been challenging. Passive nadir-viewing microwave techniques do not have sufficient resolution to resolve vertical distributions of cloud ice near tropopause heights. These observations have been limited to column measurements such as cloud liquid water path (LWP) and ice water path (IWP; e.g., Evans et al. 1998; Liu and Curry 2000; Zhao and Weng 2002). On the other hand, satellite infrared (IR) and visible limb-scan techniques (e.g., Wang et al. 1995) are dominated by diffuse (thin cirrus) clouds rather than small, opaque clouds that may contribute significant ice content. Documentation of significant convective lofting of ice to the tropical tropopause has been limited to a few in situ cases (e.g., Knollenberg et al. 1993).

Millimeter and submillimeter limb techniques offer a new opportunity for observing cloud ice near the tropopause, which are complementary to IR/visible nadir sensors in many aspects. In particular, microwave limb techniques have gained appreciable vertical resolutions to detect high clouds at different altitudes. The long horizontal pathlengths of limb sounding become very useful for surveying tropopause cloud ice with more

Corresponding author address: Dr. Dong L. Wu, Jet Propulsion Laboratory, California Institute of Technology, MS 183-701, 4800 Oak Grove Drive, Pasadena, CA 91109.
E-mail: Dong.L.Wu@jpl.nasa.gov

frequent intersections of tall and narrow clouds than that from nadir sounders. Moreover, microwave radiation can penetrate through most ice clouds and provide cloud mass information without being limited by cloud temperature, surface emission, and multiple scattering that often cause problems in other remote sensing techniques.

This paper describes a cloud detection and ice water content (IWC) retrieval technique, which has been applied to the *Upper Atmosphere Research Satellite*/Microwave Limb Sounder (*UARS*/MLS) 203-GHz radiances. The retrieval makes use of cloud-induced radiances (ΔT_{cir}) at high tangent heights (h_t) and involves a two-step calculation: ΔT_{cir} to ice water path along line of sight (hereafter hIWP) and hIWP to IWC. We focus on the MLS IWC and cloud occurrence frequency (CF) measurements for two special periods when dynamics in the TTL differ substantially: the dry (January–March 1992) and wet (July–September 1992) phases of the "tape recorder" phenomenon in the lowermost tropical stratosphere (Mote et al. 1996). MLS measures tropopause cloud ice and water vapor (Read et al. 2004) nearly simultaneously, which makes these data unique for TTL studies.

2. MLS 203-GHz observations

a. UARS/*MLS experiment*

UARS/MLS is a passive instrument with three double-sideband radiometers near 63, 183, and 203 GHz, measuring temperature (T), H_2O, O_3, and ClO profiles in the middle atmosphere (Barath et al. 1993; Waters 1993; Froidevaux et al. 1996; Livesey et al. 2003). There are 30 spectral channels in the 183-GHz radiometer and 45 channels in the 203-GHz radiometer that cover spectral ranges: 183.1–186.5 and 200.1–206.4 GHz, respectively. Compared to nadir-scanning operational microwave radiometers, the vertical field of view (FOV) of the MLS 203-GHz radiometer is narrower: ~3 km at the tangent point. The horizontal resolutions are 7 km across and ~300 km along the line of sight (LOS).

The vertical plane of the MLS scan is 90° from the satellite direction of motion, and the antenna step-scans the atmospheric limb from ~90 km to the surface in 65.5 s during normal operation. The scan interval varies from ~3 km in the stratosphere/troposphere, to ~5 km in the mesosphere. MLS radiances lack coherence when they hit clouds because of the relatively large spatial separation between adjacent measurements (vertically by ~3 km and horizontally by 15 km). With such sparse sampling MLS cannot adequately resolve deep convective clouds in either dimension. The MLS horizontal resolution is also limited by the smearing along the LOS (~300 km). MLS latitudinal coverage ranges from 34° in one hemisphere to 80° in the other as a result of the 57° orbital inclination and the instrument-viewing direction. UARS performs a 180°-yaw maneuver 10 times yr^{-1} to allow alternate observations of high latitudes every ~36 days. The MLS 203-GHz radiometer was fully operational (producing ~1300 profiles day^{-1}) between September 1991 and December 1994 before the number of daily profiles was reduced. The 183-GHz radiometer stopped collecting data in April 1993 after 18 months of successful operation. Beside the normal scan mode, MLS was also operated occasionally with a limb-tracking mode in which the FOV points at a fixed h_t (usually ~18 km).

The MLS 183- and 203-GHz radiometers together provide nearly collocated water vapor and cloud ice in the upper troposphere/lower stratosphere (UT/LS) region. The 183-GHz radiances have the best sensitivity to water vapor in the lower stratosphere (Pumphrey 1999) and in the upper-TTL region (Read et al. 2004). On the other hand, the 203-GHz channel provides the best water vapor sensitivity at 464–147 hPa (Read et al. 2001). However, these water vapor retrievals suffer from cloud contamination when scattering of ice particles is strong. Cloud-induced radiances are best detected with the 203-GHz channel and can be used for cloud ice retrieval.

b. Cloud signatures in limb radiances

Clouds can affect MLS radiances at all h_t below the cloud top but the cloud effects can vary substantially with frequency and h_t, which yield unique limb radiance measurements in many cases. The best channel for cloud detection is near the spectral window (i.e., 203 GHz for MLS) where the radiances are least affected by H_2O and O_3. Figure 1 shows MLS radiance measurements at ~203 GHz during limb-scan and limb-tracking operations. In the limb-scan case (Fig. 1a) clear-sky radiance profiles are mostly clustered in a narrow band with clear upper and lower bounds. Water vapor variabilities cause most of the radiance spread within the band. A few measurements outside the clear-sky band are indicative of thick and dense clouds where the cloud-induced radiance ΔT_{cir} (the difference from the clear-sky limit) can be as much as 30 K at $h_t = 12$ km and −130 K at $h_t < 5$ km. The instrument noise (~0.09 K) is generally negligible compared to these cloud effects. Lacking contrasts at $h_t = 8$–12 km, cloud effects become difficult to distinguish from clear-sky variability. Thus, for the best cloud detection, we have to rely on limb radiances in optically thin (at high h_t) or optically thick (at low h_t) situations. To study cloud ice near the tropopause, this paper uses the optically thin radiances exclusively.

In the 18-km limb-tracking observations (Fig. 1b), clear and cloudy radiances can be distinguished by correlation among adjacent measurements, which exhibit very different characteristics in the two cases. Clear-sky radiances vary smoothly along the orbit due to changes in tangent pressure (P_{tan}), H_2O, and T. Except for the sharp discontinuities caused by MLS-

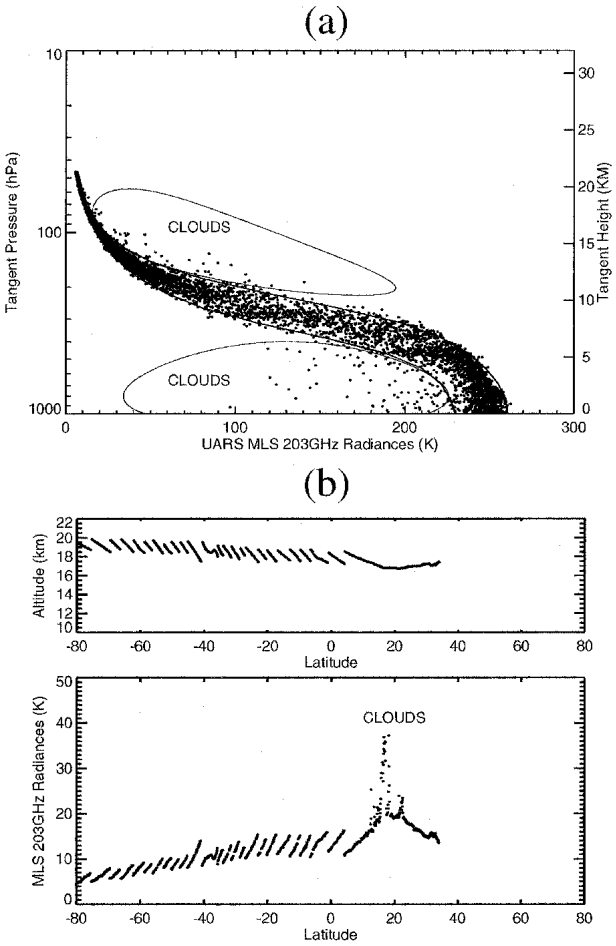

FIG. 1. *UARS*/MLS 203-GHz radiances measured during (a) limb-scan and (b) limb-tracking operations. In the limb-scan case, most of the radiances are confined in the envelopes determined by clear-sky variability. Above ~12 km tangent heights, clouds are indicated by excess radiances above the clear-sky limit, whereas at lower tangent heights they show up as radiance depressions below the clear-sky limit. Clouds are not readily detectable at intermediate tangent heights (8–12 km for 203 GHz). In the limb-tracking case, clear- and cloudy-sky radiances show very different variations in terms of horizontal scale. The large short-scale radiance fluctuations near 20°–25°N are indicative of cloud hits, whereas the more gradual radiance variations are likely due to water vapor and pointing variations. The periodic discontinuities along the orbit are caused by pointing corrections in maintaining 18-km limb tracking.

pointing adjustments, the coherence among neighboring clear-sky radiances is very high. On the other hand, cloudy radiances lack point-to-point coherence but exhibit generally higher brightness than the normal background as a whole. In this example the peak ΔT_{cir} reaches as high as ~20 K at latitudes between 15° and 20°N.

The limb ΔT_{cir} near the tropopause could arise from narrow thick and dense towers (e.g., deep convective core) or from extensive cirrus outflows. Because MLS limb measurements are separated by 15 km horizontally, the correlation between adjacent ΔT_{cir} measurements could be used to infer the sizes of cloud systems. Poor point-to-point correlation suggests that the clouds are likely to be deeply convective since their sizes are typically 10–50 km, whereas extensive cirrus anvils would produce a better point-to-point correlation. We have browsed many days of the limb-tracking data and found that MLS-sensitive clouds at the tropopause heights are mostly of convective type with a few cases blended with broad warmer-than-normal features in the brightness temperature. Long-lived, extensive thin cirrus do not contribute significantly to the MLS ΔT_{cir} because of low IWCs and small ice particles. This assertion is also in line with the result from the Mie calculation (see the appendix), where only large (100–300 μm) ice particles can produce significant volume extinction at 203 GHz. The appearance of a significant number of such large particles is generally associated with strong deep convection.

In principle, ice emission and scattering can both cause the excess radiances at $h_t > 12$ km. Scattering directs the radiation from below and above into LOS. The scattered radiance from below brings in brightness temperature radiation that is higher than the normal background, whereas the one from above brings in colder radiation (cosmic background plus downward radiation). In addition to scattering, cloud ice emission itself adds radiation to the normal background. If ΔT_{cir} is dominated by ice emission, cloud ice would behave like a gas species and the ΔT_{cir}–hIWP relation is independent of particle size distributions (PSDs). If the process is dominated by scattering, the ΔT_{cir}–hIWP relation depends on PSD, shape and ice density, as well as surface emission and cloud distribution. For the coarse sampling with *UARS*/MLS, it is not practical to retrieve IWC from hIWP on a single scan because of the required spherical homogeneity assumption. To overcome this limitation, we make regional averages of hIWP measurements on a monthly or seasonal basis, in which cloud variabilities at short temporal and spatial scales are hopefully washed out, and the spherical homogeneity assumption may be applied to the region. In this study the region for averaging hIWP is defined as a 5° × 10° latitude–longitude box, where typically 40 samples are collected for a period of 1 month in the Tropics. A similar retrieval approach was used on the Stratospheric Aerosol and Gas Experiment II (SAGE II) data where CF is averaged to overcome undersampling problems by the limb technique (Wang et al. 1995).

c. Clear- and cloudy-sky separation

The methods for cloud detection generally fall into two categories: 1) empirical approaches based on clear–cloudy-sky contrasts among adjacent measurements, and 2) model approaches to compute clear-sky limits based on radiative-transfer (RT) models. In either case, the algorithm needs to be robust and reliable

enough for handling exceptions like missing data, unknown atmospheric background, and erroneous instrument pointing. For IR limb sounding, efforts have been spent to distinguish clouds from aerosols (Kent et al. 1993). For MLS, cloud detection relies largely on the accuracy of $P_{\tan}$ and clear-sky radiance calculations.

This study chooses to use the RT method for determining clear-sky radiance and compute the 203-GHz ΔT_{cir} for each $P_{\tan}$. The clear-sky RT model is the same as used in Read et al. (2001) for upper-tropospheric H_2O retrieval, which is initialized with MLS v5 retrievals for T, $P_{\tan}$, and stratospheric H_2O and O_3 (Livesey et al. 2003). In the troposphere the National Centers for Environmental Prediction (NCEP) T is used. For the 203-GHz radiance, the sensitivity to H_2O increases with $P_{\tan}$ at 100–300 hPa, showing a dynamic range of 50–110 K at 200 hPa between very dry and very moist situations. This generally signifies poor ability for detecting clouds. To model clear-sky radiance limits at $P_{\tan}$ = 100–200 hPa, we assume $\text{RH}_i = 110\%$ for tropospheric H_2O, which accounts for ~50% supersaturation cases according to the exponential power law deduced from aircraft data (Sprichtinger et al. 2002). This RH_i threshold has a small impact on the radiance limit at 100 hPa because of insensitivity to H_2O at this level. This is shown in Read et al. (2001) and also in Fig. 1a, where the 203-GHz radiance at 100 hPa is dominated by the dry-continuum emission.

The ΔT_{cir} uncertainty depends on how well the clear-sky radiance can be modeled. As discussed in Read et al. (2001), the empirically derived 203-GHz dry and wet continuum coefficients have effectively absorbed most of the systematic biases in the NCEP T. As a consequence, the T biases do not have as much impact on the modeled radiance limit as one would expect. Figure 2a shows the ΔT_{cir} deduced from the dataset in Fig. 1a using the RT method. The sharp division in numbers of measurements between positive and negative ΔT_{cir} at high h_t suggests that the RT model method works reasonably well in separating clear- and cloudy-sky radiances. The edge of the division is blurred at $P_{\tan}$ = 200–300 hPa, reflecting increasing error in cloud detection with the RT method. Figure 2b shows the 100-hPa ΔT_{cir} histogram from 6 months of the data. The clear-sky ΔT_{cir}, fitted well to a Gaussian distribution, has a bias of 0.9 K and a standard deviation of 0.9 K at 100 hPa, due to a combination of error in $P_{\tan}$ and T, and uncounted atmospheric variabilities in H_2O, O_3, and HNO_3, etc. False cloud detection, which could introduce a bias to ΔT_{cir}, is determined by the portion of the Gaussian distribution with $\Delta T_{\text{cir}} > 3$ K. For the 3-K threshold, false detection can cause biases of 0.03 K in ΔT_{cir} and 0.9% in CF. These errors drop sharply to 0.001 K and 0.025%, respectively, when the 4-K threshold is used.

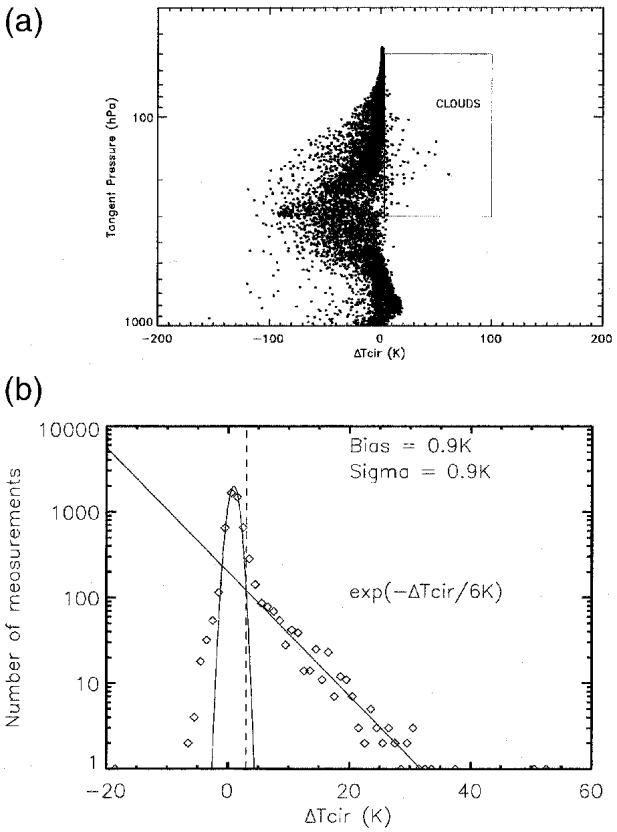

FIG. 2. (a) Cloud-induced radiances ΔT_{cir} obtained with the RT method from 1-day MLS observations. The imbedded box indicates the high h_t radiances that will be flagged as cloudy skies. As indicated by the sharp division between the number of points at $\Delta T_{\text{cir}} = 0$, the RT method works reasonably well at $P_{\tan}$ up to ~200 hPa but becomes less robust in the middle troposphere. (b) Histograms of the ΔT_{cir} at 100 hPa in connection to clear-sky radiance bias and variability. Symbols represent the number of ΔT_{cir} measurements in 1-K bins from 6 months of MLS data in early 1992 at latitudes between 25°S and 25°N. A Gaussian distribution is fitted to the clear-sky variability with the bias and standard deviation indicated in the plot. The number of cloudy-sky measurements drops off at large positive ΔT_{cir} exponentially. The 3-K cloud flag threshold is indicated by the dashed line.

3. Cloud ice retrieval

Figure 3 outlines the MLS cloud detection and retrieval algorithm scheme for measurements at high h_t. For cloud ice retrieval, we use a cloudy-sky RT (in the appendix) to obtain the ΔT_{cir}–hIWP relations. Unlike the conventional definition of nadir cloud column, hIWP represents the integral along MLS LOS, which is oriented more horizontally than vertically.

a. The ΔT_{cir}–hIWP relation

The ΔT_{cir}–hIWP relations are h_t dependent and the RT model with cloud scattering assumes spherical ice particles and PSDs from McFarquhar and Heymsfield (1997; hereafter MH97). Because of the penetration ability of the 203-GHz radiation, the calculated

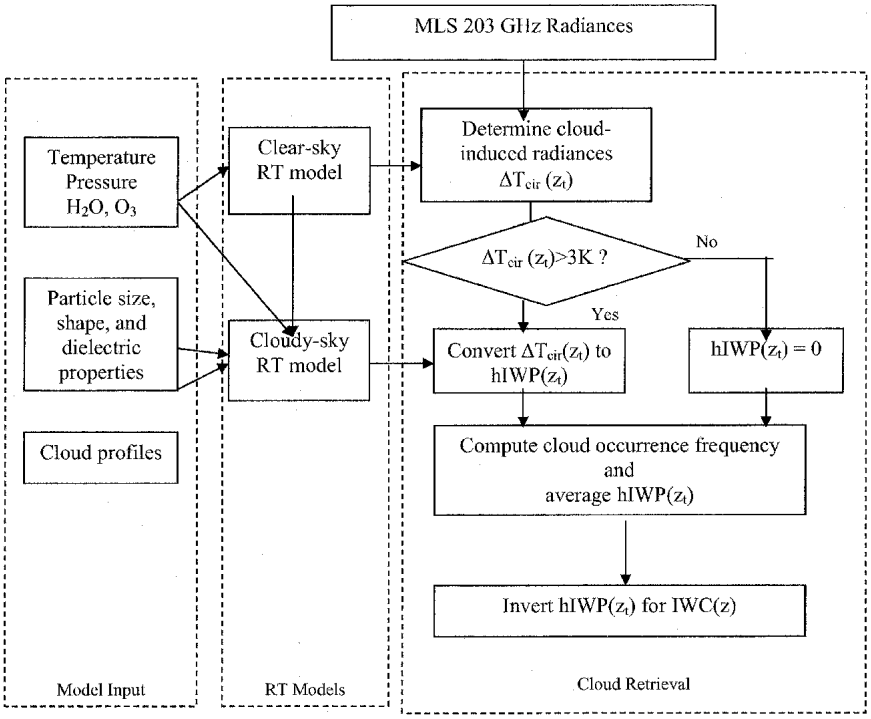

FIG. 3. MLS cloud ice retrieval scheme.

ΔT_{cir}–hIWP relation is affected little by the IWC profile used. Cloud self-extinction and air attenuation is considered in the hIWP calculation, which can become critical for low-h_t situations where cloud self-extinction is strong.

The retrieval starts by first converting ΔT_{cir} to hIWP with the modeled ΔT_{cir}–hIWP relation. This is applied independently to each measurement at h_t before they are averaged into monthly or seasonal composites. As shown in Fig. 4, the modeled ΔT_{cir}–hIWP relation is h_t dependent, varying from ~7 K kg^{-1} m^2 at ~15 km to ~11 K kg^{-1} m^2 at 11 km. The h_t dependency is caused primarily by the height-dependent PSDs in MH97.

b. IWC retrievals

The converted hIWP are averaged into eight P_{tan} bins (44.4, 58.2, 76.3, 100, 131, and 172 hPa) and 5° × 10° (latitude × longitude) grid boxes. For each grid box, IWC is retrieved from the averaged hIWPs using the onion-peeling technique and outputted at four pressure levels at 76, 100, 131, and 172 hPa. The false detection bias (0.03 K) in ΔT_{cir} would yield a ~0.05 mg m^{-3} bias in IWC at 100 hPa. The retrieved IWC is a regional mean (including both clear and cloudy cases), which is different from the regional mean single-cloud IWC. The latter is the IWC averaged only for cloudy cases that measure the average ice mass carried by a single cloud. The two quantities are related by CF, a quantity that is also derived from MLS radiance measurements.

c. IWC–ΔT_{cir} relation at 100 hPa

Because most deep convective clouds in the Tropics top out around 100 hPa, the hIWP-to-IWC inversion may not be needed at the top level. Cloudy-sky RT calculations (Fig. A3) show that the 100-hPa ΔT_{cir} is approximately proportional to IWC at 100 hPa and the

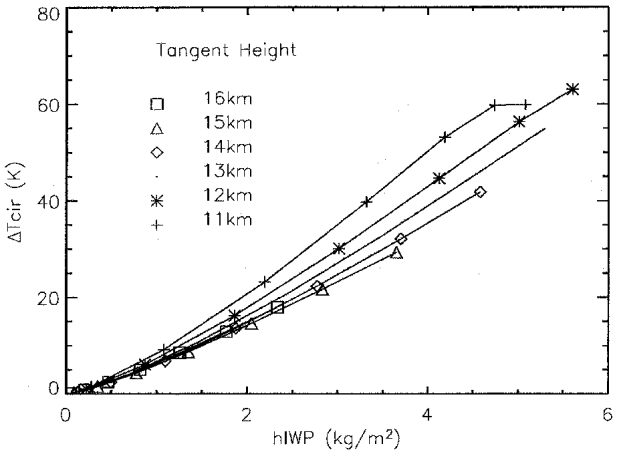

FIG. 4. The hIWP–ΔT_{cir} relations for 203-GHz limb radiance as calculated from the cloudy-sky RT model. The model uses the PSD parameterization in MH97 and assumes spherical ice particles for scattering calculations. The calculated hIWPs have been corrected for cloud self-extinction and air attenuation effects (see the text).

IWC–ΔT_{cir} relation is nearly linear ($\sim$1.5 mg m^{-3} K^{-1}) for ΔT_{cir} less than $\sim$30 K. Since the observed ΔT_{cir} are mostly less than 30 K at this level, it is valid for most cloud cases at 100 hPa to use the linear IWC–ΔT_{cir} relation for the conversion. Like the hIWP–ΔT_{cir} conversion, the IWC–ΔT_{cir} conversion suffers from the scaling error due to uncertainties about ice PSD, shape, and density.

4. Initial results

The initial studies with MLS cloud ice measurements are focused on the dry (January–March) and moist (July–September) phases of the lower stratospheric tape recorder (Mote et al. 1996). Figures 5 and 6 compare maps of T, CF, IWC, H_2O, and RH$_i$ (relative humidity w.r.t. ice) at 100 hPa for the two periods in 1992. MLS v702 H_2O (Read et al. 2004) is used to help diagnose/interpret IWC morphology. The RH$_i$ data are derived from MLS H_2O volume mixing ratio (vmr) and NCEP temperature. The following analyses are focused on the geographical distributions and temporal variations of cloud ice in relation to T, H_2O, and RH$_i$ at 100 hPa.

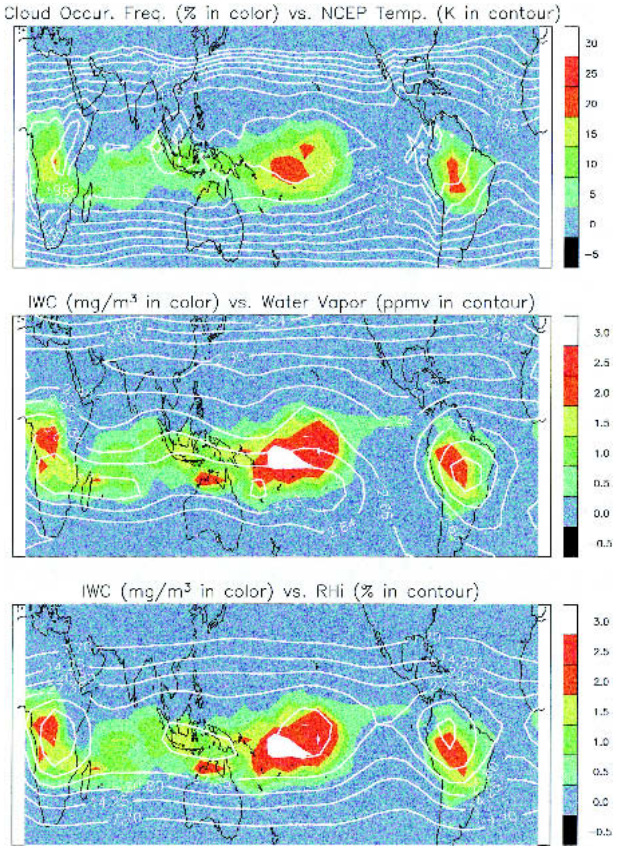

FIG. 5. Cloud ice, water vapor, and temperature maps at 100 hPa for Jan–Mar 1992. (top) MLS CF (colors) and NCEP temperature (contours). (middle) MLS IWC (colors) and H_2O vmr (contours). (bottom) MLS IWC (colors) and RH$_i$ (contours). Profiles contaminated by clouds are excluded in the water vapor and RH$_i$ maps. The estimated IWC precision and bias for these maps are $\sim$0.02 and $\sim$0.05 mg m^3, respectively.

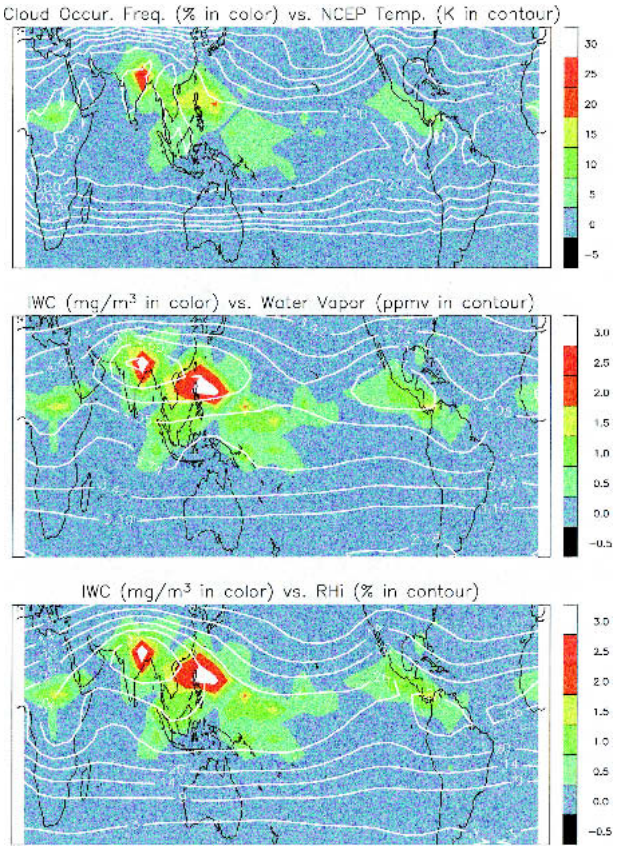

FIG. 6. As in Fig. 5 but for Jul–Sep 1992.

a. *Dry period (January–March 1992)*

During the dry period the 100-hPa IWC and CF exhibit clear maxima near the intertropical convective zones (ITCZ). The CF map agrees well with overshooting cloud morphology observed by the Tropical Rainfall Measuring Mission (TRMM) Precipitation Radar (Alcala and Dessler 2002). The maximum 100-hPa IWC in this seasonal average reaches $\sim$3 mg m^{-3}, which coincides with the CF peak ($\sim$20%). Deep convective regions over South America and South Africa have less ice mass at 100 hPa with a maximum of $\sim$2 mg m^{-3} in IWC and $\sim$20% in CF. Over northern Australia and the Southeast Asian archipelagos, there are some scattered occurrences with IWC around 1–1.5 mg m^{-3}.

The comparison with NCEP T shows that the cold (less than 198 K) regions are associated with the high 100-hPa IWCs but shifted slightly in latitude. Generally speaking, the regions, with temperature less than 198 K exhibit good symmetry about the equator and cover a much larger area than cloud ice. Despite the latitudinal shift, the longitudinal temperature variations (2–4 K)

correlate well with the modulations of IWC. These characteristics are consistent with comparisons between MLS IWC and the United Kingdom Met Office (UKMO) temperature (not shown).

At 100 hPa the IWC patterns differ noticeably from the H_2O vmr, especially in the southern subtropical Pacific where the high vmr belt is ~5°–10° southward of the IWC band. This shift between these two maximum locations implies that the water vapor band is even farther away from the center of the cold temperature region in the central Pacific. The vapor vmr and cloud ice distributions at 100 hPa appear to have larger deviations over oceans than over land masses. However, the 100-hPa IWC patterns are found to correlate significantly better with MLS 147-hPa vapor vmr (not shown) where no obvious latitudinal shift is found in the southern Pacific.

In the Northern Hemisphere, there exists a low (~2.3 ppmv) H_2O vmr band around ~25°N latitude across most longitudes with a slightly wider region over Central America. This low vmr band also exists but appears wider at 147 hPa where the moist band in the Southern Hemisphere shrinks and vanishes eventually at 215 and 316 hPa (not shown). The similar H_2O distribution repeats during the period of January–March 1993. Over South America and South Africa, IWC and H_2O vmr are well correlated but the locations of their maxima remain slightly shifted.

There is a better correlation between the IWC and RH_i patterns at 100 hPa. However, there are some noticeable differences. For example, the peak RH_i is found slightly north of the IWC maximum over South America, but aligned closely over South Africa. The 100-hPa RH_i over the central Pacific is lower than those over land masses, whereas the opposite is true for the 100-hPa IWC for land–ocean differences. This appears in line with the finding of Sherwood (2002) that continental cumulus clouds have smaller crystal sizes, which would reduce their microwave scattering potential, but increase their ability to moisten the tropopause region. However, caution is required when interpreting RH_i here since it depends on NCEP temperatures. The average RH_i is far below saturation at 100 hPa near the cloudy regions, varying between 25% and 40%, which is mostly due to the biases in MLS H_2O retrieval (Read et al. 2004) and NCEP temperature (Randel et al. 2000).

b. Moist period (July–September 1992)

During the moist period (Fig. 6) the 100-hPa IWC pattern is dominated by the contributions from Indian monsoons and typhoon systems in Southeast Asia. Deep convective systems produce up to 8-K modulations in NCEP T across the 25°N latitude band. The UKMO T indicates similar but somewhat smaller (4–6 K) perturbations at this latitude band (not shown). Again, the region with 100-hPa temperature lower than 200 K, centered on the equator, covers most of the Tropics and subtropics. The cold region is strongly perturbed by the Asian and American monsoons, pushing the envelope north to ~40°N. Like in the dry period, longitudinal temperature variations seem well correlated with IWC.

Compared to the Asian monsoon, the Central American monsoon contributes much smaller IWC at 100 hPa. A similar amount of contribution is found over central Africa and the western Pacific. Unlike in the dry period, the correlation between IWC and H_2O vmr at 100 hPa is generally good in most places, particularly near the Indian and Central American monsoons, showing peaks of 3 mg m^{-3} in IWC and ~5 ppmv in H_2O vmr. Away from the deep convective zones, there is no obvious dry latitude band in the Southern Hemisphere (winter hemisphere) where the vmr decreases monotonically with latitude.

Overall, IWC in the wet period correlates better with RH_i at 100 hPa than with the other fields. The monsoons over India, Asia, Central America, and Africa produce RH_i of 25%–40% at 100 hPa with the highest RH_i over the Indian and Asian region. There are strong latitudinal RH_i and temperature gradients north of the Indian monsoon as deep convective activity pushes far north from the equator. The cloud ice maxima over Japan, Central America, and Africa coincide with high RH_i, but not necessarily with peak RH_i values.

c. Seasonal variations

The temporal behavior of MLS IWC and H_2O is dominated by seasonal variations, and exhibits strong latitude dependence as shown in Fig. 7. Here, the 100-hPa IWC and H_2O data are limited to the early period of the *UARS* mission (September 1991–April 1993) when both MLS 183- and 203-GHz radiometers were operating.

MLS 100-hPa ΔT_{cir} (used as a cloud ice proxy) resembles the seasonal cycle of deep convective activity in the middle troposphere very well, varying around the equator within ±10° in latitude. Rough conversion from ΔT_{cir} to IWC at 100 hPa can be carried out with the 1.5 mg m^{-3} K^{-1} factor based on the in situ studies (Fig. A3). The average 100-hPa IWC between 30°S and 30°N is ~0.07 mg m^{-3}, which does not vary significantly during 1991–1997. This IWC value would yield an equivalent ~0.7 ppmv water vapor in the same region, a significant portion of the total water budget in the tropical tropopause. The IWC seasonal variation is consistent with MLS H_2O at 147 hPa, which is expected for the moistening from convective outflows at the bottom of the TTL. However, the latitudinal spread of the 147-hPa H_2O is slightly wider than that of the 100-hPa IWC.

The seasonal variation of the 100-hPa H_2O differs substantially from that of the 100-hPa cloud ice. This level is affected both by convection (Dessler 2002) and by the stratospheric circulation (Yulaeva et al. 1994),

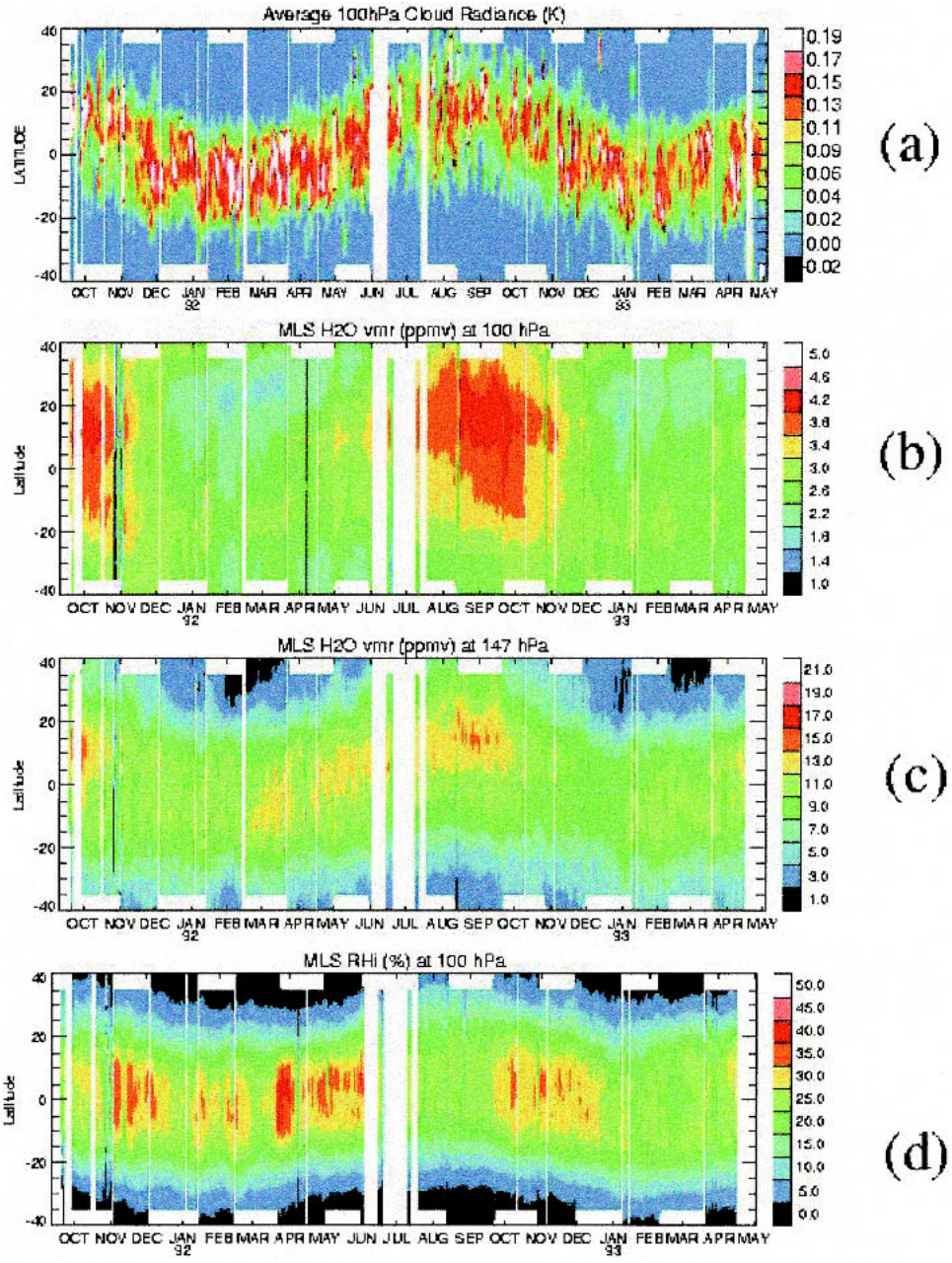

FIG. 7. The time series of (a) 100-hPa MLS cloud radiance, (b) 146-hPa MLS H_2O vmr, (c) 100-hPa MLS H_2O vmr, and (d) 100-hPa MLS RH_i. The cloud radiance is used to estimate IWC variations at 100 hPa. As described in section 3, the radiance can be approximately converted to 100-hPa IWC using the factor of 1.5 mg m^{-3} K^{-1}. For the 100-hPa H_2O vmr and RH_i results, cloudy profiles are excluded from the averaging. The white stripes represent missing data. In the RH_i time series, sudden increases or decreases in value are likely the retrieval errors as RH_i becomes sensitive to temperature uncertainty at this level.

and the H_2O seasonal cycle reflects variations in both of these processes. The interactions between convection and synoptic circulations in the UT/LS region are complex and depend on many variables, such as microphysical properties of the clouds as well as ambient relative humidity (Sherwood 2002; Sherwood and Dessler 2003). A comprehensive explanation and quantification of the distribution of these variables will have to await further theoretical and observational studies.

The moisture variation exhibits a very different pattern when expressed in RH_i instead of H_2O vmr. Because of the strong dependence of RH_i on temperature,

most of the RH_i variations result from the latitudinal and seasonal variations of temperature. The temperature error must be considered seriously in this analysis because of nonlinearity of the Clausius–Clapeyron equation. A 1-K error in temperature would yield a relative error of 17% in RH_i at 100 hPa, and therefore, conclusions based on RH_i variations should be treated with caution.

5. Discussion

Scattering calculations based on the MH97 PSDs (see the appendix) suggest that most of the 203-GHz ΔT_{cir} at tropopause heights are induced by ice particles of diameters between 100 and 300 μm. These are much larger than sizes expected for subvisible cirrus formed in situ (Jensen et al. 1996), but are typical for clouds near deep convective cores where the updraft velocity is strong enough to lift large particles to the upper troposphere. Thus, we believe that the MLS cloud ice represents mostly deep convective clouds, which are beyond, and therefore complementary to, the capability of IR and visible techniques. This inference is also consistent with the observed localization of the ice distribution relative to that of relative humidity, and with the large ice mixing ratios inferred.

However, a large uncertainty arises when converting MLS ΔT_{cir} to IWC because the 203-GHz radiances are only sensitive to ice particles of the large-size mode that may only contribute half of the total IWC (see the appendix). Assumptions about ice particle size and shape distributions are therefore critical for connecting the ice scattering sensed by MLS to the ice mass. As shown in the appendix, a bimodal PSD can complicate the IWC retrieval by having more degrees of freedom in PSD.

MLS IWC uncertainty is mostly in scaling error, not bias, as a result of the ΔT_{cir}-to-hIWC conversion. It should not have a large impact on the correlation and distribution studies as shown above. Table 1 summarizes the estimated scaling differences for the ΔT_{cir}–IWC conversion at 100 hPa with different PSDs. The derived IWC can differ by a factor of 2 to 3 depending on the PSD used. The MH97 PSD parameterization was developed from aircraft observations of deep convective outflows during the Central Equatorial Pacific Experiment (CEPEX). The MH97 work incorporates the effects of the size-dependent bulk density of ice particles in their parameterization in terms of mass-equivalent spheres. It produces clear bimodal distributions for a large IWC near the tropopause. However, the dataset lack measurements inside convective cores. In the case of strong turbulence/mixing during convective updraft, the PSD inside convective cores may differ substantially from those measured in the outflows. Strong overshooting cases can yield updraft velocities as high as 20 m s^{-1} (e.g., Geerts et al. 2000), with which ice particles can be readily mixed over several kilometers. As a result, deep convective clouds at 100 hPa may have a PSD similar to those at lower altitudes. Such PSD mixing between vertical cloud layers, as shown in Table 1 for the $-60°$ and $-75°$C cases, would result in 30% differences in IWC, which is relatively small compared to the differences caused by using different PSD parameterizations.

TABLE 1. The average 100-hPa IWC converted from MLS 203-GHz ΔT_{cir} using different PSDs. The differences reflect uncertainties in current PSD parameterizations in the upper troposphere, which in turn limits the accuracy of MLS IWC retrieval. The term D_{mm} is the mass–mean diameter, weighted by the cubic power of particle diameter.

	T (°C)	D_{mm} (μm)	IWC (mg m^{-3})
McFarquhar and Heymsfield (1997)	−60	114	0.056
	−75	103	0.075
Heymsfield et al. (2002)	−60	143	0.056
	−75	73	0.201
Liu and Curry (1998)	−60	64	0.123
	−75	56	0.171

PSD can be height dependent and sometimes IWC dependent as suggested by MH97. Liu and Curry (1998) studied essentially the same CEPEX dataset but came up with a slightly different PSD parameterization. The primary difference between the MH97 and Liu–Curry parameterizations is the assumption about particles with diameter <100 μm, which turns out to be critical for IWC retrievals at 203 GHz. The Liu–Curry parameterization produces a smaller mass-mean diameter for the same temperature and hence a larger MLS IWC. Heymsfield et al. (2002) compiled a parameterization by fitting height-dependent gamma distributions to in situ measurements in the Tropics and subtropics at $T > -55$°C. The MLS IWC from this parameterization at -60°C yields the same result as one from the MH97 PSD despite different mass–mean diameters. The Heymsfield et al. (2002) result at -75°C may be negligible because it is extrapolated from the measurements at lower altitudes. The lack of reliable PSD information renders a large scaling error as high as 100%–200% for the IWC at 100 hPa. In addition, Evans and Stephens (1995) argued that assumptions about ice particle shape and density are as equally important as PSD under extreme conditions. It is not clear, however, what are the statistical orientations of different particle shapes and how significant the radiance polarization differences can be at 203 GHz. A recent study showed an encouraging agreement between collocated in situ and remotely sensed (radar) IWC measurements with biases <20% (D. Sayres 2003, personal communication). This result has important implications to both passive and active cloud remote sensing methods since they all depend on PSD assumptions. It is easy to find a large number of collocated satellite measurements for calibrating IWCs obtained from space radar and passive

sensors, but the radar–in situ matches are difficult to find and remain very sparse. We anticipate that the accuracy for remotely sensed IWC will continuously be improved as more in situ IWC measurements are collected from future suborbital or underflight platforms. Nevertheless, reducing uncertainties associated with particle size, shape, and ice density remains a major challenge in future cloud observations.

Despite the existing uncertainty, MLS IWC observations from the 203-GHz radiances are unique and no previous estimates exist for global convective cloud ice at the tropopause. The cloud ice maps and seasonal variations contain useful information for improving our understanding of the processes in the TTL. Because of the penetrative ability of microwave radiation, the 203-GHz limb radiance demonstrates an adequate dynamic range for measuring thick and dense clouds in the TTL, particularly those from deep convection. Thus, cloud inhomogeneity becomes less a problem than in optically saturated cases, and the hIWP–ΔT_{cir} relation depends little on cloud location along LOS.

The existence of significant cloud ice in the TTL has an important implication to the understanding of mass transport at high altitudes. The "slow ascent" models like Holton and Gettelman (2001), Jensen and Pfister (2004), and others have been emphasizing transport controlled by large-scale flows, but did not consider mass transport by convection above the lowest levels of the TTL, except for the effects of convection on the temperature structure of the TTL. The MLS observations, which despite the large uncertainties, are unique and show that convection is important throughout the TTL. This suggests that the slow ascent models need to be modified to take into account the existence of convection extending throughout the TTL.

6. Summary and future work

The initial IWC retrievals from the 203-GHz radiances, together with MLS water vapor measurement and NCEP temperature data, reveal many interesting features related to interactions between deep convective clouds and tropopause dynamics. These results can be summarized as follows:

1) The average 100-hPa IWC between 30°S and 30°N is ~0.07 mg m^{-3} during 1991–97, which is obtained assuming the MH97 PSD in cloud scattering calculations. This IWC would yield ~0.7 ppmv for equivalent water vapor in the same region, a significant portion of the total water budget in the tropical tropopause. Seasonal IWC means may reach up to 30 ppmv vapor equivalent over convective areas, far exceeding the vapor mass at this level. However, these IWC values must be treated with caution due to potential scaling error of 200%–300% from PSD and particle shape uncertainties. But even with a factor of 3 error, peak IWC values must dominate the total water content at 100 hPa over some deep convective regions, confirming the importance of convectively lofted ice to the water budget up to the tropical cold point.
2) There is a generally good correlation between IWC and RH_i at 100 hPa in both seasonal extremes. However, ice distributions are more localized and often offset from RH_i maxima, suggesting that deep convection is the dominant source of the observed local RH_i variability, as expected from radiative transfer arguments. Ice maxima over land areas tend to be moister than those over oceans, suggesting dynamical or microphysical differences between the cloud systems.
3) In general, MLS IWC distribution patterns correlate positively with the water vapor vmr at 100 hPa except near the southern Pacific during the dry period (e.g., January–March 1992), where the vmr peak is located 5°–10° south of the IWC. Better correlation is found when comparing the 100-hPa IWC to the 147-hPa H_2O vmr.

A new MLS instrument, that was launched on the National Aeronautics and Space Administration (NASA) *Aura* satellite in July 2004 has frequency channels similar to *UARS* MLS with a number of additions near 118, 190, 240, 640 GHz and 2.5 THz. The broader bandwidths and high-rate h_t sampling (every ~0.4 km) from the new instrument will provide much improved data in the upper troposphere (Waters et al. 1999). In particular, we plan to use the *Aura* 240- and 640-GHz measurements to study the 100-hPa cloud ice, and hopefully to reduce uncertainty by comparing them to IWC measurements from CloudSat 94-GHz Cloud Profiling Radar (CPR; due to launch in 2005). *Aura* MLS and CloudSat CPR, flying in formation as part of NASA's "A" train, will have comparable footprints with samples taken within 7 min of each other. The new data will help to resolve some issues not adequately addressed with the *UARS* data.

Acknowledgments. We thank Dr. Joe Waters for valuable comments and Dr. Gloria Manney for providing the NCEP and UKMO temperature data. AED and SCS acknowledge an EOS Interdisciplinary Science grant to the University of Maryland and Yale University. This research was performed at the Jet Propulsion Laboratory, California Institute of Technology, under contract with NASA.

APPENDIX

Cloudy-Sky RT Model

The RT model that we use to calculate MLS 203-GHz cloudy radiances is briefly described in the following. The radiative transfer equation we solve along the LOS can be written as

$$\frac{dT_b}{ds} = -\beta_e T_b + \beta_a \hat{T} + \beta_s T_{\text{scat}}, \qquad \text{(A1)}$$

where s is distance along the LOS, T_b is microwave radiance in Kelvin, and β_e, β_a, and β_s are total volume extinction, absorption, and scattering coefficients, respectively, in units of m^{-1} (e.g., Ulaby et al. 1981). The first source function $\hat{T}$ represents emission and is equal to air temperature T under the Rayleigh–Jeans approximation. The second source function T_{scat} accounts for the radiances scattered into the LOS by clouds. For simplicity, we neglect the polarization properties of cloud scatterers, and assume spherical ice particles. The atmosphere is divided into spherically stratified layers with vertically varying gases and cloud variables (temperature, density, ice water content, etc.).

Equation (A1) can be evaluated by separate downward and upward integrals. For the downward path, the integration is carried out from the top of model atmosphere to the tangent point (or the surface if the tangent height is below the surface), and the upward path integration is carried out from the tangent point (or the surface) to the top of the atmosphere.

The scattering processes are assumed to be independent (or incoherent) among different cloud hydrometeors so that the total scattered radiances can be expressed as the sum of contributions from different particles (van de Hulst 1981). Cloud ice particles are also assumed to be made of pure water with density $\rho_{\text{ice}} = 0.91$ g cm^{-3}, and uncertainties in ρ_{ice} will cause a scaling error in the modeled ΔT_{cir}–hIWP relation. The Mie theory is applied to calculate phase functions and scattering coefficients for each particle size. The model uses the MH97 PSD parameterization and includes only ice particles between 0 and 4000 μm in diameter.

Figure A1 shows relative contribution to IWC and volume extinction/scattering coefficients (β_{c_e}/β_{c_s}) at 203 GHz from unit size bin with a MH97 PSD. Since IWC and scattering are proportional to the third and sixth moment of the PSD, respectively, the bimodal size distribution plays a key role in partitioning IWC between those from diameters <100 μm and those from >100 μm. As indicated by the relative β_{c_s} contribution from unit size bins, or $d\beta_{c\_s}/dr$, the 203-GHz radiances provide better sensitivity at diameters >100 μm. However, these large particles may not dominate the total IWC according to the MH97 PSD parameterization. In this example the ratio of the 203-GHz sensitivity, that is, $\beta_{c\_e}(2r < 100\mu\text{m}) : \beta_{c\_e}(2r > 100\mu\text{m})$, is 1:7, whereas the ratio of $\text{IWC}(2r < 100\mu\text{m}) : IWC(2r > 100\mu\text{m})$ is nearly 1:1.

The source functions T_{scat} are calculated using an iterative approach for each cloud layer (e.g., Wilheit et al. 1982). These are localized sources and therefore we may assume plane-parallel geometry for the calculations. Figure A2 illustrates the coordinates for the T_{scat} calculation, where the scattering volume is placed at the

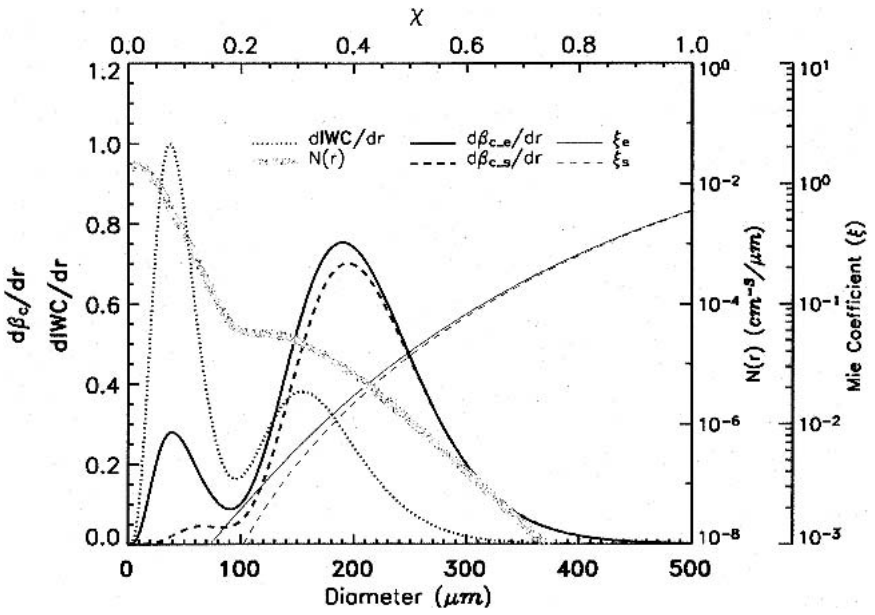

FIG. A1. Size dependence of IWC and volume scattering/extinction coefficients. Here, $N(r)$ is number density of ice particle as a function of radius, and this bimodal PSD is from the MH97 parameterization for IWC = 0.01 g m^{-3} and $T = -60°$. The relative contribution of IWC and volume extinction/scattering coefficients (β_{c_e}/β_{c_s}) from unit size bin, i.e., $d\text{IWC}/dr$ and $d\beta_{c\_e}/dr$, or $d\beta_{c\_s}/dr$, have arbitrary units. For particles of size <100 μm the volume extinction is dominated by ice absorption, whereas it is mainly due to scattering if particle sizes are greater than 100 μm.

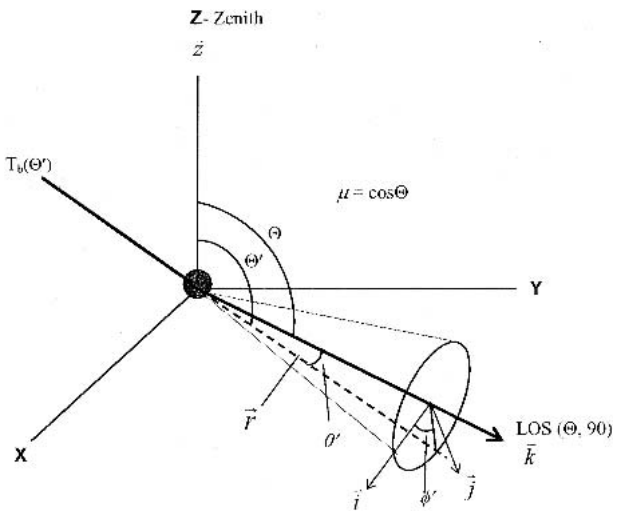

FIG. A2. Diagram to illustrate the geometry of cloud scattering calculation in the limb RT model.

origin, the z axis is zenith, and the LOS lies in the y–z plane with angle Θ from zenith and $\Phi = 90°$ from x axis. The incident radiance T_b with zenith angle Θ' is a function of θ, ϕ and Θ, where angles (θ, ϕ) are the angular coordinates with respect to the LOS. Since the incident T_b is only a function of Θ' for the plane-parallel atmosphere, the expression for T_{scat} can be simplified to the following

$$T_{\text{scat}}(\Theta) = \frac{1}{2}\int_0^{\pi} P(\theta')\overline{T}_b(\theta')\sin\theta' d\theta' \qquad \text{(A2)}$$

and

$$\overline{T}_b(\theta') = \frac{1}{2\pi}\int_0^{2\pi} T_b(\theta', \phi')d\phi' = \frac{1}{2\pi}\int_0^{2\pi} T_b(\Theta')d\phi',$$

where θ' is the scattering angle between Θ and Θ', and ϕ' is the azimuth angle that lies in the plane perpendicular to the LOS. The angle Θ' can be expressed in terms of θ', ϕ', and Θ as

$$\cos\Theta' = \mathbf{r}\cdot\mathbf{z} = \sin\theta'\sin\Theta\sin\phi' + \cos\theta'\cos\Theta,$$

where $\mathbf{r}$ and $\mathbf{z}$ are the unit vectors of the incident radiance and the zenith directions, respectively. Here, $\overline{T}_b(\theta')$ is evaluated at each layer for all zenith angles Θ' from the surrounding radiation. For the angular integrations, the model uses 16 θ streams and 8 ϕ streams on 0.125-km vertical grids. This configuration produces less than 1% error in the 200-GHz limb radiances under typical convective clouds.

Iterations for the T_{scat} calculation begin by first initializing all the downward radiances to 0 K and all the upward radiances to 300 K. Using the initial radiances, T_{scat} are evaluated with Eq. (A2) and then substituted into the RT Eq. (A1) to compute a new set of downward and upward radiances. The next iteration repeats Eq. (A2) and Eq. (A1) calculations but with the new radiance set. The final equilibrium T_{scat} is obtained until convergence (0.1 K) is found. These source functions are evaluated independently for each cloud layer. Once all these source functions are finalized, they are incorporated into the RT equation for limb geometry to calculate limb radiances.

Figure A3a shows the limb radiance profiles calculated from a deep convective cloud with various IWCs. An ideal cloud profile model is used between 5 and 17 km where IWC decreases exponentially (~4-km scale height) with height. The IWC values labeled in the figure indicates the peak value at 5 km. The ΔT_{cir} can saturate as the cloud becomes very thick. The ΔT_{cir}–IWC relation at 100 hPa (Fig. A3b) shows a near linear dependence at IWC < 40 mg m^{-3} and saturation at IWC > 100 mg m^{-3}.

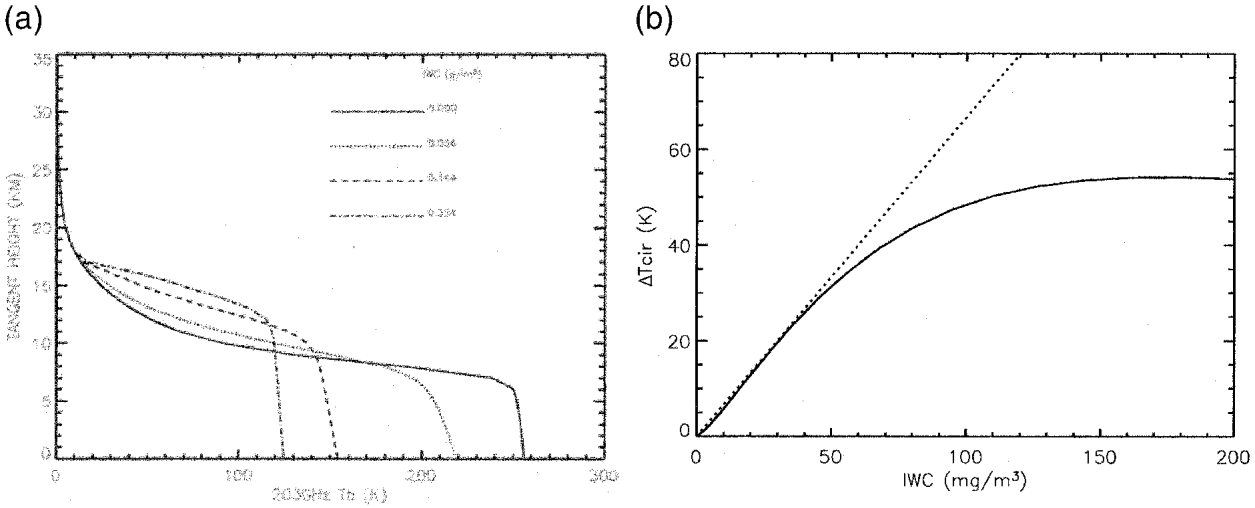

FIG. A3. (a) The 203-GHz radiance profiles calculated for deep convective clouds with different IWCs. (b) The calculated ΔT_{cir}–IWC relation at 100 hPa. The dotted line shows the slope of 1.5 mg m^{-3} K for IWC < 40 mg m^{-3}. Optically thick clouds cause the ΔT_{cir} saturated to ~55 K.

REFERENCES

Alcala, C. M., and A. E. Dessler, 2002: Observations of deep convection in the tropics using the TRMM precipitation radar. *J. Geophys. Res.,* **107,** 4792, doi:10.129/2002JD002457.

Barath, F., and Coauthors, 1993: The Upper Atmosphere Research Satellite Microwave Limb Sounder instrument. *J. Geophys. Res.,* **98,** 10 751–10 762.

Danielsen, E. F., 1982: A dehydration mechanism for the stratosphere. *Geophys. Res. Lett.,* **9,** 605–608.

Dessler, A. E., 1998: A reexamination of the "stratospheric fountain" hypothesis. *Geophys. Res. Lett.,* **25,** 4165–4168.

——, 2002: The effect of deep, tropical convection on the tropical tropopause layer. *J. Geophys. Res.,* **107,** 4033, doi:10.1029/2001JD000511.

Evans, K. F., and G. L. Stephens, 1995: Microwave radiative transfer through clouds composed of realistically shaped ice crystals. Part I: Single scattering properties. *J. Atmos. Sci.,* **52,** 2041–2057.

——, S. J. Walter, A. J. Heymsfield, and M. N. Deeter, 1998: Modeling of submillimeter passive remote sensing of cirrus clouds. *J. Appl. Meteor.,* **37,** 184–205.

Froidevaux, L., and Coauthors, 1996: Validation of UARS Microwave Limb Sounder ozone measurements. *J. Geophys. Res.,* **101,** 10 017–10 060.

Geerts, B., G. M. Heymsfield, L. Tian, J. E. Halverson, A. Guillory, and M. I. Mejia, 2000: Hurricane Georges' landfall in the Dominican Republic: Detailed airborne Doppler radar imagery. *Bull. Amer. Meteor. Soc.,* **81,** 999–1018.

Heymsfield, A. J., A. Bansemer, P. R. Field, S. L. Durden, J. L. Srith, J. E. Dye, W. Hall, and C. A. Grainger, 2002: Observations and parameterizations of particle size distributions in deep tropical cirrus and stratiform precipitating clouds: Results from in situ observations in TRMM field campaigns. *J. Atmos. Sci.,* **59,** 3457–3491.

Holton, J. R., and A. Gettelman, 2001: Horizontal transport and dehydration in the stratosphere. *Geophys. Res. Lett.,* **28,** 2799–2802.

Jensen, E. J., and L. Pfister, 2004: Transport and freeze-drying in the tropical tropopause layer. *J. Geophys. Res.,* **109,** D02207, doi:10.1029/2003JD004022.

——, O. B. Toon, H. B. Selkirk, J. D. Spinhirne, and M. R. Schoeberl, 1996: On the formation and persistence of subvisible cirrus clouds near the tropical tropopause. *J. Geophys. Res.,* **101,** 21 361–21 375.

Kent, G. S., D. M. Winker, M. T. Osborn, and K. M. Skeens, 1993: A model for the separation of cloud aerosol in SAGE II occultation data. *J. Geophys. Res.,* **98,** 20 725–20 735.

Knollenberg, R. G., K. Kelly, and J. C. Wilson, 1993: Measurements of high number densities of ice crystals in the tops of tropical cumulonimbus. *J. Geophys. Res.,* **98,** 8639–8664.

Liu, G., and J. A. Curry, 1998: Remote sensing of ice water characteristics in tropical clouds using aircraft microwave measurements. *J. Appl. Meteor.,* **37,** 337–355.

——, and ——, 2000: Determination of ice water path and mass median particle size using multichannel microwave measurements. *J. Appl. Meteor.,* **39,** 1318–1329.

Livesey, N. J., and Coauthors, 2003: The UARS Microwave Limb Sounder version 5 dataset: Theory, characterization and validation. *J. Geophys. Res.,* **108,** 4378, doi:10.1029/2002JD002273.

McFarquhar, G. M., and A. J. Heymsfield, 1997: Parameterization of tropical cirrus ice crystal size distributions and implications for radiative transfer: Results from CEPEX. *J. Atmos. Sci.,* **54,** 2187–2200.

Mote, P. W., and Coauthors, 1996: An atmospheric tape recorder: The imprint of tropical tropopause temperatures on stratospheric water vapor. *J. Geophys. Res.,* **101,** 3989–4006.

Newell, R. E., and S. Gould-Stewart, 1981: A stratospheric fountain? *J. Atmos. Sci.,* **38,** 2789–2796.

Pumphrey, H. C., 1999: Validation of a new prototype water vapor retrieval for the UARS Microwave Limb Sounder. *J. Geophys. Res.,* **104,** 9399–9412.

Randel, W. J., F. Wu, and D. J. Gaffen, 2000: Interannual variability of the tropical tropopause derived from radiosonde data and NCEP reanalyses. *J. Geophys. Res.,* **105,** 15 509–15 523.

Read, W. G., and Coauthors, 2001: UARS MLS upper tropospheric humidity measurements: Method and validation. *J. Geophys. Res.,* **106** (D23), 32 207–32 258.

——, D. L. Wu, J. W. Waters, and H. C. Pumphrey, 2004: A new 147-68 hPa water vapor product from the UARS Microwave Limb Sounder. *J. Geophys. Res.,* **109,** D06110, doi:10.1029/2003JD004056.

Sherwood, S. C., 2002: A microphysical connection among biomass burning, cumulus clouds, and stratospheric moisture. *Science,* **295,** 1272–1275.

——, and A. E. Dessler, 2000: On the control of stratospheric humidity. *Geophys. Res. Lett.,* **27,** 2513–2516.

——, and ——, 2003: Convective mixing near the tropical tropopause: Insights from seasonal variations. *J. Atmos. Sci.,* **60,** 2674–2685.

Sprichtinger, P., K. Gierens, and W. G. Read, 2002: The statistical distribution law of relative humidity in global tropopause region. *Meteor. Z.,* **11,** 83–88.

Ulaby, F. T., R. K. Moore, and A. K. Fung, 1981: *Microwave Remote Sensing: Active and Passive.* Vol. I, *Microwave Remote Sensing Fundamentals and Radiometry,* Artech House, 456 pp.

van de Hulst, H. C., 1981: *Light Scattering by Small Particles.* Dover, 470 pp.

Wang, P.-H., M. P. McCormick, P. Minnis, G. S. Kent, G. K. Yue, and K. M. Skeens, 1995: A method for estimating vertical distribution of the SAGE II opaque cloud frequency. *Geophys. Res. Lett.,* **22,** 243–246.

Waters, J. W., 1993: Microwave limb sounding. *Atmospheric Remote Sensing by Microwave Radiometry,* M. A. Janssen, Ed., John Wiley and Sons, 572 pp.

——, and Coauthors, 1999: The UARS and EOS Microwave Limb Sounder Experiments. *J. Atmos. Sci.,* **56,** 194–218.

Wilheit, T. T., and Coauthors, 1982: Microwave radiometric observations near 19.35, 95, and 183 GHz of precipitation in Tropical Storm Cora. *J. Appl. Meteor.,* **21,** 1137–1145.

Yulaeva, E., J. R. Holton, and J. M. Wallace, 1994: On the cause of the annual cycle in tropical lower-stratospheric temperatures. *J. Atmos. Sci.,* **51,** 169–174.

Zhao, L., and F. Weng, 2002: Retrieval of ice cloud parameters using the Advanced Microwave Sounding Unit. *J. Appl. Meteor.,* **41,** 384–395.